ACS OMEGA

http://pubs.acs.org/journal/acsodf

Article

Fabrication of Mesoporous PtO−ZnO Nanocomposites with Promoted Photocatalytic Performance for Degradation of Tetracycline

Reda M. Mohamed,* Adel A. Ismail,* Mohammad W. Kadi, Ajayb S. Alresheedi, and Ibraheem A. Mkhalid

Cite This: *ACS Omega* 2021, 6, 6438−6447

Read Online

ACCESS | Metrics & More | Article Recommendations

ABSTRACT: Herein, we report a simple incorporation of PtO NPs at diverse percentages (0.2−0.8 wt %) onto a highly crystalline and mesoporous ZnO matrix by the wet-impregnation approach for degradation of tetracycline (TC) upon visible light exposure. These well-dispersed and small-sized PtO NPs provide the mesoporous PtO−ZnO nanocomposites with outstanding photocatalytic performance for complete TC degradation. The optimized 0.6% PtO−ZnO photocatalyst exhibits excellent TC degradation, and its degradation efficiency reached ∼99% within 120 min. The photocatalytic performance of the 0.6% PtO−ZnO nanocomposite is 20 and 10 times higher than that of pristine ZnO and commercial P-25, respectively. The photodegradation rate of TC over the 0.6% PtO−ZnO nanocomposite is 34 and 12.5 times greater than that of pristine ZnO and commercial P-25, respectively. This is because of the large surface area, unique porous structure, synergistic effect, and broad visible light absorption of the PtO−ZnO nanocomposite. Moreover, mesoporous PtO−ZnO nanocomposites showed a high stability and recyclability over five iterations. This work demonstrates the remarkable role of combining PtO and ZnO photocatalysts in providing nanocomposites with significant potential for the preservation of human health through wastewater remediation.

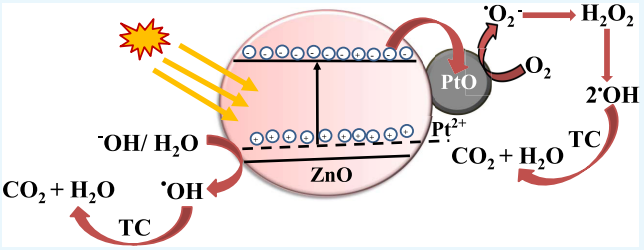

1. INTRODUCTION

Semiconductor ZnO exhibits unique properties such as a wide band gap, large surface area, cost effectiveness, high chemical stability, and suitable positions of band edges in terms of the redox potentials for detoxification of organic compounds and hydrogen production.[1−4] ZnO, as an efficient photocatalyst compared to TiO_2, has a higher harvest efficiency under UV illumination and shows little absorption of the solar spectrum.[5,6] ZnO is comparatively plentiful, considering the evaluated reserves of zinc of about 230 million tonnes in mining areas of the earth.[7] There has been considerable interest in the photocatalysis application of ZnO, in particular upon UV illumination; however, it cannot work well in visible light illumination; thus, scientists have been making efforts to overcome its shortcomings.[8,9] To extend the photoactivity and photoresponse of ZnO in the broad visible light absorption (∼43% of the solar spectrum),[10] its band structures are modified to promote H_2 generation and detoxification of organic compounds.[11] This modification was carried out through several routes comprising doping noble metals, doping non-metal or metal ions, incorporating with narrow bandgap oxides such as Bi_2O_3 and Fe_2O_3, and dye sensitization.[12−16]

Precious metals like Pd, Pt, Au, and Ag and their oxide-based catalysts with high photocatalytic activity are considered as outstanding catalysts and are considerably employed in diverse industrial applications,[17] predominately nanosized noble metals with high utilization efficiency and excellent photocatalytic performance.[18,19] Among noble metals, Pt and its oxide-based catalysts have excellent catalytic, chemical, and physical, properties, therefore possessing enormous research utilities.[20−23] In the past 20 years, environmental pollution and global energy issues have encouraged significant development in photoelectric conversion and the photochemistry approach.[24−28] As part of the fundamental research in electrophotochemistry, the ZnO photocatalyst has been employed and studied in photocatalytic degradation of various organic compounds and H_2 generation from water splitting.[29−34] Upon light illumination, semiconductor materials are excited to create photogenerated holes with oxidizability and the

Received: January 8, 2021
Accepted: February 17, 2021
Published: February 23, 2021

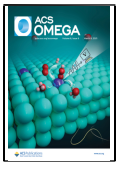

https://dx.doi.org/10.1021/acsomega.1c00135
ACS Omega 2021, 6, 6438−6447

corresponding electrons with reducibility, and all of these migrate to the surface of the semiconductor materials.[35]

Antibiotics, in particular tetracycline, in water circumstances are commonly originated from domestic sewage, hospitals, industrial waste, and poultry farms.[35] Due to the antibiotics' stability in terms of chemical structure in aqueous solution, it is hard to eliminate them through conventional treatment and biodegradation processes.[36] TC has received considerable attention as a representative antibiotic widely found in domestic wastewater. The remaining TC is eliminated by different approaches such as photocatalysis, advanced oxidation, adsorption, etc.[37−39] Recently, the photocatalytic destruction of organic contaminants in aqueous solution has been considered a favorable avenue and environment-friendly green path, which directly destructs into innoxious products.[38,39] With the popular use and despite the disadvantage of antibiotics, they have become critical due to their inherent resistance to bacteria, leading to intimidation to environmental pollution and global health. In the past 20 years, many research studies in photocatalytic degradation by employing different photocatalysts have attempted to synthesize appropriate, effective photocatalysts through visible light to benefit potential large-scale applications. Generally, the preparation strategies of the photocatalysts include an expensive organic stabilizer, a time-consuming process, and/or sophisticated equipment, thus emphasizing the need for further development. Consequently, it is important to fabricate an effective and simple procedure for obtaining a PtO−ZnO photocatalyst with high photocatalytic performance and well-defined structure.

Herein, we report a simple method of incorporation of PtO NPs onto a highly crystalline and mesoporous ZnO matrix by the wet-impregnation method for photocatalytic degradation of TC upon visible light exposure. The optimized 0.6% PtO−ZnO photocatalyst exhibits an excellent degradation efficiency of TC, reaching ∼99%. The photocatalytic performance of the 0.6% PtO−ZnO nanocomposite is 20 and 10 times higher than that of pristine ZnO and commercial P-25, respectively. The photodegradation rate of TC over the 0.6% PtO−ZnO nanocomposite is 34 and 12.5 times greater than that of pristine ZnO and commercial P-25, respectively. The rate constant of the 0.6% PtO−ZnO nanocomposite was 48 and 18 times higher than that for pristine ZnO NPs and commercial P-25, respectively.

2. EXPERIMENTAL SECTION

2.1. Materials. $Pt(NH_3)_4(NO_3)_2$, CH_3COOH, $Zn(NO_3)_3{\cdot}6H_2O$, C_2H_5OH, HCl, and nonionic surfactant Pluronic F-108 with M_n ∼14 600 were acquired from Sigma-Aldrich.

2.2. Construction of Mesoporous PtO−ZnO Nanocomposites. A typical synthesis of mesoporous ZnO matrix was as follows: 0.2 g of F-108 surfactant was dissolved in 30 mL of C_2H_5OH with magnetic stirring for 60 min to get a clear solution. Then, 0.74 mL of HCl and 2.3 mL of CH_3COOH were added to the F-108 solution with stirring for 60 min. Finally, 20.3 g of $Zn(NO_3)_3{\cdot}6H_2O$ was added to the mesophase including F-108. The sol was kept at 40 °C with the humidity at 40% to polymerize the mesophase to get the gel construction and thus dried at 65 °C for 12 h prior to calcination at 450 °C for 4 h. Mesoporous PtO−ZnO nanocomposites were fabricated as follows: 1 g of mesoporous ZnO matrix with a high surface area was suspended in 100 mL of C_2H_5OH. The desired concentration of $Pt(NH_3)_4(NO_3)_2$ was gradually obtained using the mesoporous ZnO NP matrix by agitation for 60 min. Subsequently, the aqueous solution was evaporated at 110 °C for 12 h and followed by calcination at 400 °C for 3 h to collect mesostructured 0.2, 0.4, 0.6, and 0.8 wt % PtO−ZnO nanocomposites.

2.3. Characterization. XRD patterns were determined using the Bruker AXS D4 Endeavour X diffractometer. TEM images were examined by a JEOL JEM-2100F electron microscope. N_2 adsorption−desorption isotherms were measured using the Quantachrome Autosorb equipment at 77 K after outgassing at 200 °C for 12 h. A spectrofluorophotometer (RF-5301 PC, 400 W, 50/60 Hz) was used to measure the photoluminescence (PL) by employing a xenon lamp (150 W) as the excitation source at $\lambda \sim 365$ nm. Spectra obtained by X-ray photoelectron spectroscopy (XPS) were analyzed using a Thermo Scientific K-Alpha spectrometer. The Zahner Zennium electrochemical workstation was employed to determine the transient photocurrent measurements. The system comprised a standard three-electrode Pt wire as the counter electrode and a calomel electrode as the reference electrode; the synthesized samples were used as working electrodes immersed in 0.1 M Na_2SO_4 as the electrolyte. A 500 W xenon lamp was applied as the UV−vis light source. Spectra were recorded using a Perkin Elmer Fourier transform infrared spectrometer (FT-IR) at 400−4000 cm^{-1}. Diffuse reflectance spectra were determined at $\lambda \sim 200$−800 nm by applying a Varian Cary 100 Scan UV−vis system.

2.4. Photocatalytic Test. The photodegradation of TC (20 mg L^{-1}) over mesoporous PtO−ZnO nanocomposites at different percentages of PtO NPs was carried out upon visible light exposure. A 300 W xenon lamp with a wavelength λ of <420 nm was fixed above the photoreactor (250 mL) at 10 cm distance. The mesoporous PtO−ZnO nanocomposites were sonicated in 200 mL of aqueous TC solution (20 mg L^{-1}) with air pumping, used as an O_2 source. In the dark, the suspension was stirred for 30 min to obtain the adsorption equilibrium of TC. The photocatalytic efficiency of the mesoporous PtO−ZnO nanocomposites was determined for 2 h of illumination. The photodegradation efficiency was estimated by TC analysis by employing a spectrophotometer with an absorbance peak at 361 nm after separating the liquid by a 0.22 μm nylon filter at the regular time. % Photodegradation efficiency = $(C_0 - C_t)/C_0 \times 100\%$, where C_t and C_0 are the TC concentrations at a specific time t and zero time, respectively. Also, the mesoporous PtO−ZnO nanocomposite was reused for five further experiments to verify the recyclability and stability of the synthesized photocatalytic material.

3. RESULTS AND DISCUSSION

The XRD patterns of pristine ZnO NPs and mesoporous PtO−ZnO nanocomposites at diverse PtO percentages as depicted in Figure 1 correspond to the hexagonal wurtzite ZnO structure (JCPDS no. 36-1451).[40] The pristine ZnO NPs are highly crystalline with sharp peaks. The well-defined diffraction peaks of hexagonal wurtzite ZnO at the crystal planes of (100), (002), (101), (102), (110), (103), (200), (112), and (201) correspond to 2θ = 31.7, 34.2, 36.2, 47.6, 56.6, 62.8, 66.5, 67.9, and 69.3°, respectively. Besides, narrow XRD peaks with strong diffraction are observed, as shown in Figure 1, indicating the high crystallinity of the mesoporous PtO−ZnO nanocomposites. Furthermore, no distinct peaks were detected from the impurities, precursors, or other ZnO phases, demonstrating the high ZnO purity when synthesized

https://dx.doi.org/10.1021/acsomega.1c00135
ACS Omega 2021, 6, 6438−6447

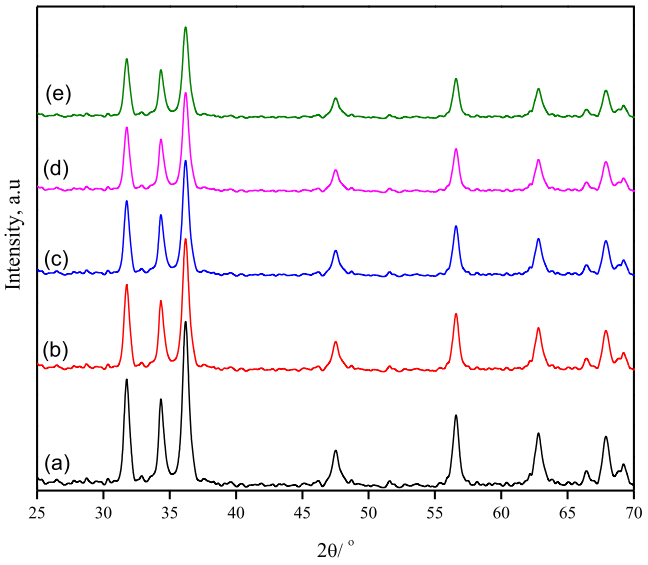

Figure 1. X-ray diffraction for mesoporous ZnO nanoparticles (a). PtO−ZnO nanocomposites at varying PtO contents: 0.2 wt % (b), 0.4 wt % (c), 0.6 wt % (d), and 0.8 wt % (e). Shifted for sake of clarity.

using the present procedure. The XRD patterns of the mesoporous PtO−ZnO nanocomposites show similar diffraction peaks to those of the pristine ZnO NPs (Figure 1), indicating that the hexagonal wurtzite ZnO is the main structure for all synthesized samples. Besides, there are no overserved diffraction peaks due to the presence of PtO NPs or Pt, which is owing to their high dispersion on the mesoporous ZnO matrix, small size, and low concentration (0.2−0.8 wt %). However, it is observed that the peak intensities of the mesoporous PtO−ZnO nanocomposites are significantly smaller than those of the pristine ZnO NPs.

The N_2 adsorption−desorption isotherms of pristine ZnO and the mesoporous 0.6% PtO−ZnO nanocomposite are evaluated as displayed in Figure 2A to estimate the pore size distribution and surface area. At a high relative pressure (P/P_0), the isotherm for N_2 adsorption of pristine ZnO is higher than that of the 0.6% PtO−ZnO nanocomposite. It is observed that both isotherms with H2 hysteresis loops can be categorized as the IV type, which is distinctive of mesostructured materials.[41] The surface area of the mesoporous 0.8% PtO−ZnO nanocomposite (125 m^2 g^{-1}) is smaller than that of pristine ZnO NPs (140 m^2 g^{-1}), which also explains the fractional incorporation of the PtO NPs onto the mesoporous ZnO matrix during calcination (Table 1). The pore size of the pristine ZnO was determined to be 4.82 nm, which was slightly reduced (4.6 nm) for the 0.8% PtO NPs as a result of PtO incorporation. The pore sizes and surface area of all synthesized photocatalysts are tabulated in Table 1. The increased surface areas of the mesoporous PtO−ZnO nanocomposites in the present work are considered the best values compared to those previously reported; they could adsorb TC molecules more readily, supply more reactive sites onto the synthesized samples, and thus promote the photocatalytic efficiency. The FT-IR spectra of the PtO−ZnO nanocomposites at different PtO percentages are depicted in Figure 2B. The broad peaks for the pristine ZnO and PtO−ZnO nanocomposites were located at 3220−3550 cm^{-1}, matching the O−H stretching vibration, and the peak located at 1634.90 cm^{-1} is attributed to the bending modes of the hydrated oxide surface and adsorbed H_2O.[42,43] The Zn−O vibration peak was observed at 784 cm^{-1}. After incorporating PtO onto mesoporous ZnO, the characteristic Zn−O vibration peak

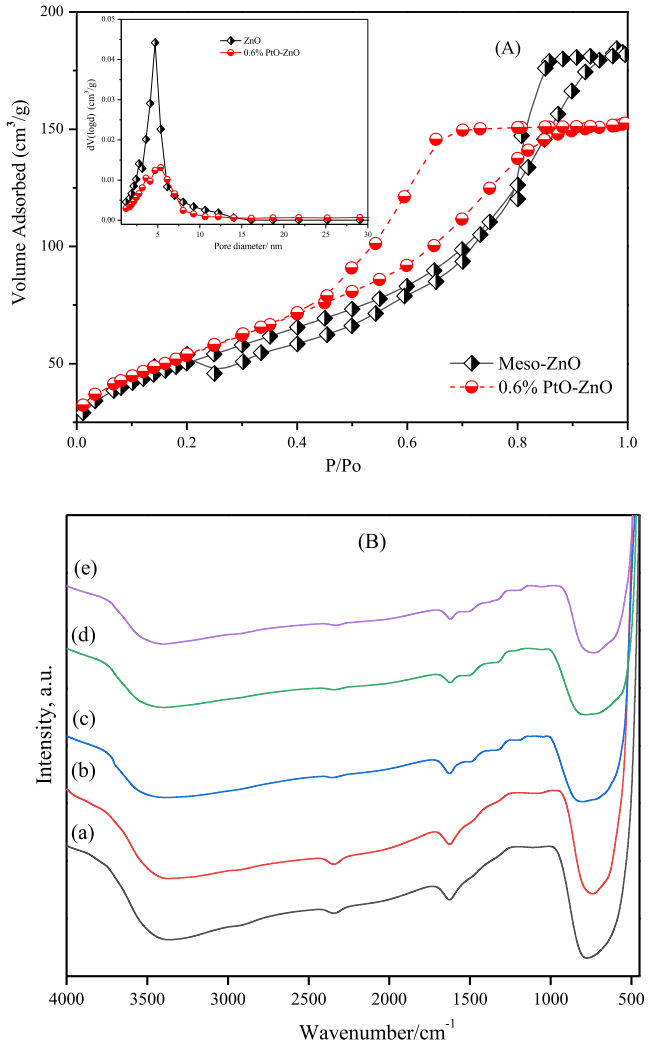

Figure 2. (a) N_2 sorption isotherms of the mesoporous ZnO nanoparticles and 0.6 wt % PtO−ZnO nanocomposite; (b) FTIR spectra of the mesoporous ZnO nanoparticles (a) and mesoporous PtO−ZnO nanocomposites at varying PtO contents: 0.2 wt % (b), 0.4 wt % (c), 0.6 wt % (d), and 0.8 wt % (e). Shifted for sake of clarity.

Table 1. Physical Properties of Pristine ZnO NPs and Mesoporous PtO−ZnO Nanocomposites at Different Percentages of PtO and Their Photodegradation of Tetracycline upon Visible Light Illumination[a]

photocatalysts	S_{BET} (m^2 g^{-1})	band gap (eV)	pore size (nm)	rate constant k (min^{-1})	r (μmol g^{-1} min^{-1})
meso-ZnO	140	3.18	4.82	0.0010	0.035
0.2% PtO−ZnO	138	2.99	4.74	0.0077	0.360
0.4% PtO−ZnO	133	2.70	4.68	0.0195	0.865
0.6% PtO−ZnO	129	2.36	4.6	0.0482	1.216
0.8% PtO−ZnO	125	2.35	4.6	0.0515	1.420
P-25	50	3.20		0.0026	0.097

[a] S_{BET} surface area, and r photodegradation rate of tetracycline.

https://dx.doi.org/10.1021/acsomega.1c00135
ACS Omega 2021, 6, 6438−6447

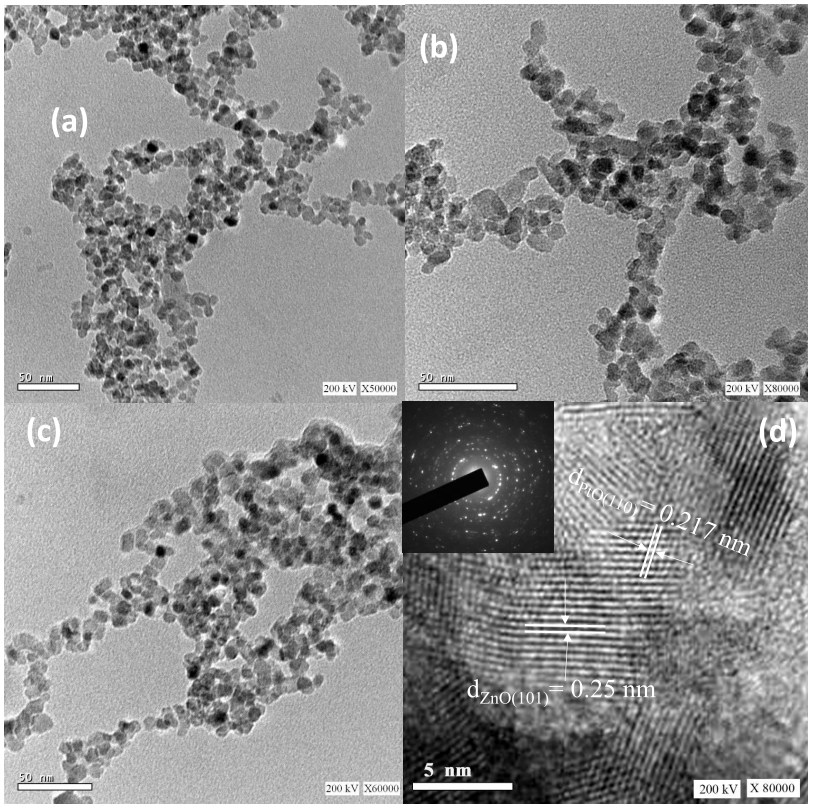

Figure 3. TEM images of mesoporous ZnO nanoparticles (a); 0.6 wt % PtO−ZnO (b) and 0.8 wt % PtO−ZnO nanocomposites (c); HRTEM image of 0.6 wt % PtO−ZnO nanocomposite (d).

was gradually shifted to ∼743 cm^{-1} with the increment of PtO NPs from 0.2 to 0.8%, which confirms the coexistence of ZnO and PtO NPs and confirms the construction of PtO−ZnO nanocomposites. The intensity of the Zn−O peak was reduced for the synthesized PtO−ZnO nanocomposites compared with pristine ZnO NPs, indicating the replacement of Pt(II) on the mesoporous ZnO matrix.[44]

TEM images for the pristine ZnO NPs and mesoporous 0.6 and 0.8% PtO−ZnO nanocomposites were examined as displayed in Figure 3. Figure 3a shows that the ZnO NPs were highly dispersed, with an entirely uniform shape and size and average particle sizes of ∼5−10 nm. Figure 3b,c reveals the TEM of 0.6 and 0.8% PtO−ZnO nanocomposites. The images show that PtO−ZnO particles with average particle sizes of ∼5−10 nm were not agglomerated after incorporating PtO NPs of completely uniform shape and size. The HR-TEM image of the mesoporous 0.6% PtO−ZnO nanocomposite shows that the distances between two close planes were 0.25 and 0.217 nm, indicating the presence of (101) and (110) planes for ZnO and PtO with high crystallinity, which is satisfactory for the immigration of charge carriers[45] (Figure 3d). The particle size of the PtO NPs is around ∼3 nm (Figure 3d). Selected area electron diffraction showed polycrystalline ZnO hexagonal construction as displayed in Figure 3d, inset.

X-ray photoelectron spectroscopy (XPS) of the mesoporous 0.6% PtO−ZnO nanocomposite was done to evaluate the chemical state as displayed in Figure 4a−c. XPS of the Pt 4f spectrum of PtO−ZnO as depicted in Figure 4a showed that the two characteristic peaks of Pt $4f_{7/2}$ and Pt $4f_{5/2}$ appeared at binding energies of 72.6 and 75.9 eV, respectively, indicating the existence of the chemical state of Pt(II) and further demonstrating the incorporation of PtO NPs onto the mesoporous ZnO matrix.[46] Furthermore, it is shown that PtO NPs incorporated on the mesoporous PtO−ZnO nanocomposites are typically deposited on the surface of the ZnO matrix. Figure 4b exhibits two main peaks of the Zn 2p XPS spectrum; the peaks located at 1021.6 and 1044.7 eV are attributed to Zn(II) $2p_{3/2}$ and Zn^{2+} $2p_{1/2}$, respectively, which indicates the formation of the Zn^{2+} state. The variance between Zn $2p_{3/2}$ and Zn $2p_{1/2}$ in terms of binding energy is estimated at around 23.1 eV.[47] The XPS of the O 1s spectrum exhibits one main peak located at 530.1 eV as depicted in Figure 4c, indicating the presence of the lattice oxygen of Zn−O and Pt−O.[48] XPS of the mesoporous 0.6% PtO−ZnO nanocomposite revealed that the final product's weight percentages are compatible with the Pt_2O/ZnO ratio and the atomic percentages of the Pt, Zn, and O are determined to be 0.55, 54.07, and 45.38%, respectively.

To evaluate the optical performances of the newly synthesized pristine ZnO NPs and mesoporous PtO−ZnO nanocomposites at different PtO percentages, diffuse reflectance UV−vis spectra (DRS) were determined (Figure 5). The absorbance edge of pristine ZnO NPs showed a broad peak in the UV region at 300−400 nm (Figure 5a). However, mesoporous PtO−ZnO nanocomposites exhibited the absorption edge from 400 to 600 nm within the visible absorbance range, as depicted in Figure 5a. Defect sites could explain this enhanced visible light harvest in the wide region as due to the presence of O^{2-} vacancies in the lattices. Therefore, the increment of PtO percentages leads to a decrease in the bandgap energies. In addition, for calculation of the direct bandgap energy (E_g) of the synthesized samples, the relation between photon energy and $(\alpha h\nu)^2$ was analyzed by applying the equation $(\alpha h\nu)^2 = A(h\nu - E_g)$, where A is the absorbance

https://dx.doi.org/10.1021/acsomega.1c00135
ACS Omega 2021, 6, 6438−6447

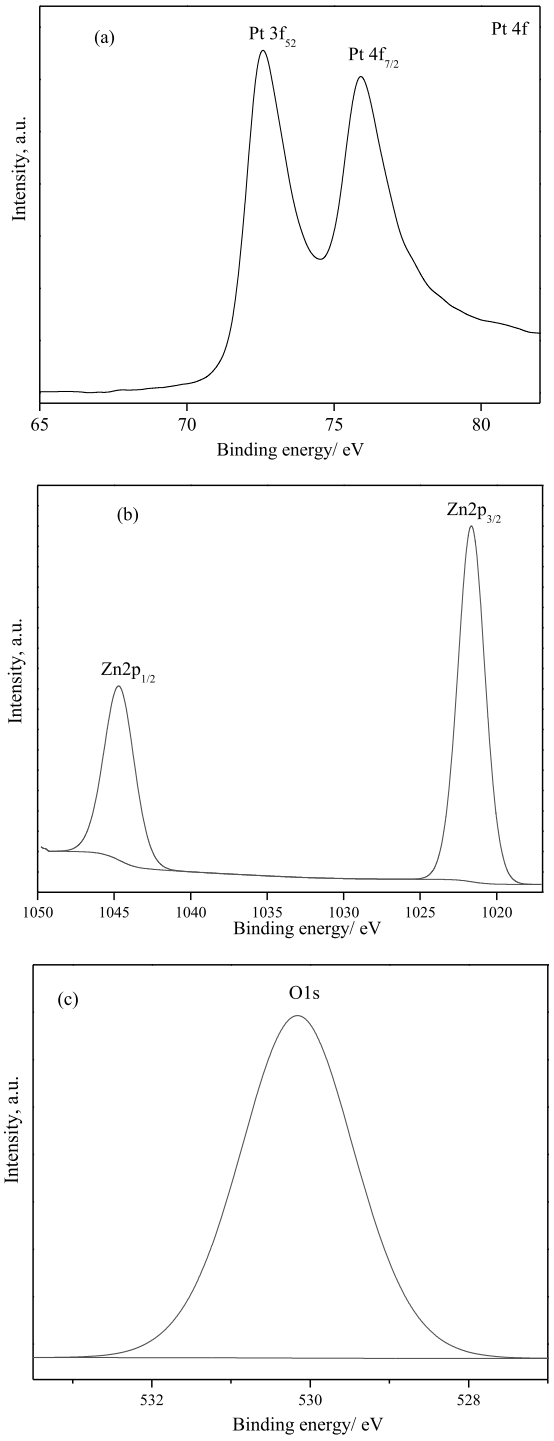

Figure 4. XPS analysis of the 0.6 wt % PtO−ZnO nanocomposite emerging from the emissions of the Zn, Pt, and O elements; Pt 4f (a), Zn 2p (b), and O 1s (c).

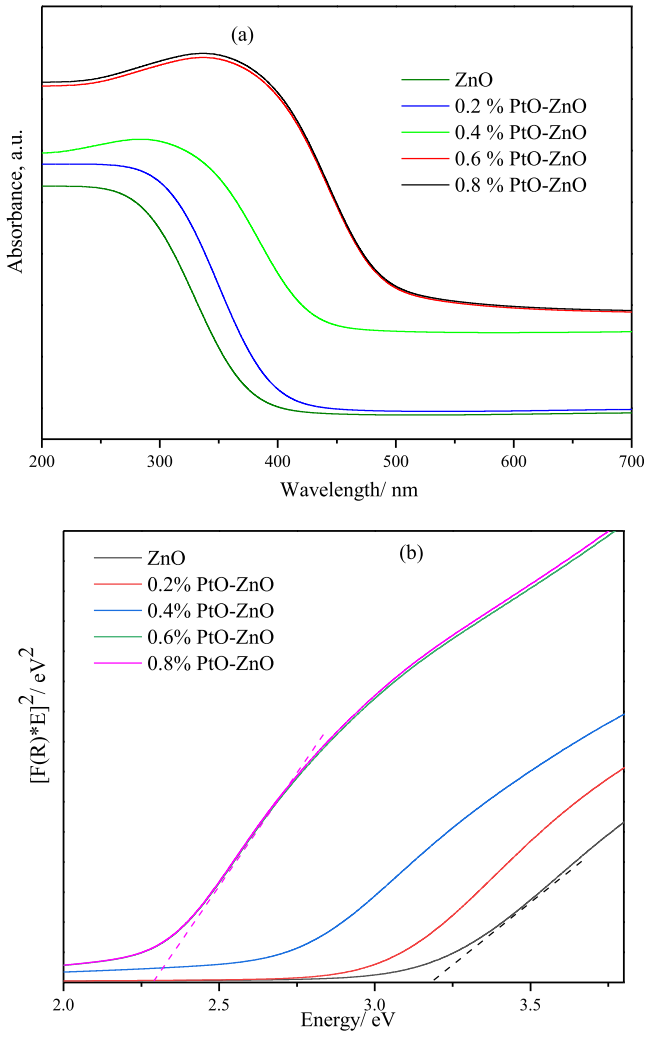

Figure 5. (a) Diffuse reflectance spectra of mesoporous ZnO nanoparticles and mesoporous PtO−ZnO nanocomposites at varying PtO contents (0.2−0.8 wt %); (b) plot of transferred Kubelka−Munk versus the energy of the light absorbed for mesoporous ZnO nanoparticles and mesoporous PtO−ZnO nanocomposites at varying PtO contents (0.2−0.8 wt %).

constant, E_g is the bandgap energy, and $h\nu$ is the incident photon energy. The E_g value was derived from the Tauc plot in Figure 5b by the linear tangential versus $h\nu$ axis. The bandgap values for pristine ZnO, and 0.2, 0.4, 0.6, and 0.8% PtO−ZnO nanocomposites are estimated to be around 3.18, 2.99, 2.70, 2.36, and 2.35 eV, respectively (Table 1). The reduction of the band gap and red shift in the absorption upon PtO incorporation onto the mesoporous ZnO matrix are owing to the electronic transformations from the ZnO band edge to Pt(II) NPs.

3.1. Photocatalytic Degradation of TC. The photocatalytic performances of mesoporous PtO−ZnO nanocomposites at various PtO percentages were assessed by TC degradation under ambient conditions during visible light exposure illumination to commercial P-25 and pristine ZnO NPs. The photolysis of TC without a photocatalyst was carried out for 120 min of illumination as a blank control. The results exhibited nearly no TC degradation without photocatalysts upon illumination, and the photolysis of TC was determined to be less than 2% for within 120 min. However, the maximum adsorption capacity of TC over mesoporous PtO−ZnO nanocomposites was determined to be around 5−10% for 120 min. Figure 6a indicates that the incorporation of PtO NPs onto the mesoporous PtO−ZnO nanocomposites increases the photocatalytic efficiency for degradation of TC through visible light exposure for 120 min. It is revealed that the photocatalytic efficiency enhancement of mesoporous PtO−ZnO nanocomposites is mainly produced from the incorporation of

https://dx.doi.org/10.1021/acsomega.1c00135
ACS Omega 2021, 6, 6438−6447

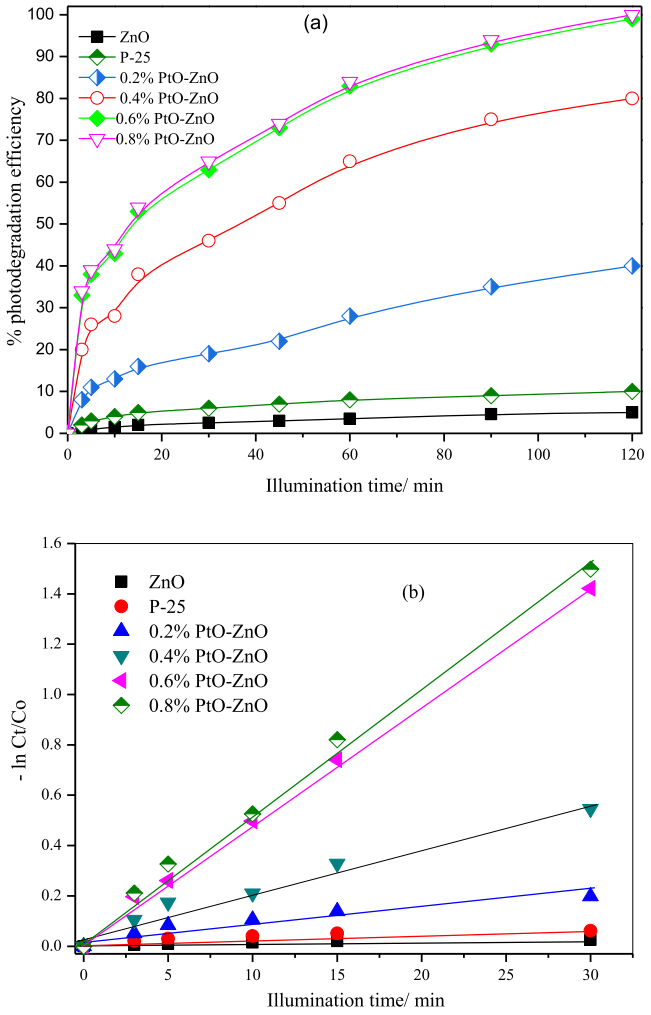

Figure 6. (a) Time courses of the photodegradation of tetracycline over mesoporous ZnO NPs and mesoporous PtO−ZnO nanocomposites at varying PtO contents (0.2−0.8 wt %) compared with commercial P-25 under visible light. (b) Linear relationship between the illumination time and $\ln(C_0/C_t)$, where C_0 and C_t are the TC concentrations at zero time and a specific time t, respectively, during photodegradation of tetracycline over mesoporous ZnO NPs and mesoporous PtO−ZnO nanocomposites at varying PtO contents (0.2−0.8 wt %) compared with commercial P-25 under visible light (photocatalyst dose = 1 g L^{-1}, volume of aqueous solution = 100 mL, and TC concentration = 20 mg L^{-1}).

PtO NPs onto PtO−ZnO nanocomposites compared to pristine ZnO or commercial P-25. The photocatalytic efficiency over mesoporous PtO−ZnO nanocomposites was significantly improved, and their efficiency reached 40, 80, 99, and 100% for 0.2, 0.4, 0.6, and 0.8% PtO−ZnO nanocomposites compared to undoped ZnO (5%) and commercial P-25 (10%) through visible light exposure. It was revealed that the photocatalytic performance of the 0.6% PtO−ZnO nanocomposite is 20 and 10 times greater than that of the pristine ZnO NPs and commercial P-25, respectively. The photodegradation rate of TC over 0.2, 0.4, 0.6, and 0.8% PtO−ZnO nanocomposites was calculated to be 0.360, 0.865, 1.216, and 1.420 μmol g^{-1} min^{-1} compared to pristine ZnO NPs (0.035 μmol g^{-1} min^{-1}) and commercial P-25 (0.097 μmol g^{-1} min^{-1}). The photodegradation rate of TC over the 0.6% PtO−ZnO nanocomposite is 34 and 12.5 times greater than that of pristine ZnO and commercial P-25, respectively. In Figure 6b, to evaluate the TC degradation rate constant k upon visible light illumination, $\ln(C_t/C_0)$ was plotted versus illumination time t, where C_t and C_0 are the TC concentration after a certain time t and zero time, respectively, and k is the apparent rate constant. According to the equation $\ln(C_t/C_0) = -kt$, a fitting model of pseudo-first order was applied to determine the k values. As displayed in Figure 6b, all synthesized mesoporous PtO−ZnO nanocomposites are figured out to have a quite longitudinal interdependence of time and $\ln(C_t/C_0)$ (Figure 6b). The k values for mesoporous 0.2, 0.4, 0.6, and 0.8% PtO−ZnO nanocomposites were determined to be ∼0.0077, 0.0195, 0.0482, and 0.0515 min^{-1}, respectively. However, the k values for pristine ZnO NPs and commercial P-25 were 0.001 and 0.0026 min^{-1}, respectively. The k value of the 0.6% PtO−ZnO nanocomposite was 18 and 48 times higher than that for commercial P-25 and pristine ZnO NPs, respectively. Meanwhile, this calculated k value could help to determine the degradation rate of TC in the aqueous solution; plausibly the k values of 0.6 and 0.8% PtO−ZnO nanocomposites were high in terms of photocatalytic efficiency. The 0.6 and 0.8% PtO−ZnO nanocomposites revealed much higher photocatalytic efficiency than either pristine ZnO NPs or commercial P-25. As exhibited, the 0.6 and 0.8% PtO−ZnO nanocomposites show outstanding photocatalytic performance by achieving nearly full TC degradation within 120 min. Ultimately, the photocatalytic efficiency noted follows the trend 0.8% PtO−ZnO ≥ 0.6% PtO−ZnO > 0.4% PtO−ZnO > 0.2% PtO−ZnO > TiO_2-P25 > ZnO NPs. Such high photocatalytic performance of the mesoporous PtO−ZnO nanocomposites in comparison with pristine ZnO NPs and commercial P-25 could be explained by diverse factors, such as an accumulated $^{\bullet}OH$ concentration,[49] a broad visible light absorption, a narrow band gap, a lower light scattering, or a rapid transfer and facile diffusion of the TC molecule through the porous structure, which for the commercial P-25 is suppressed by the bulk sample. In addition, the mesoporous PtO−ZnO nanocomposites could reduce the recombination of carriers and hence enhance the TC photodegradation efficiency compared to the pristine ZnO NPs and commercial P-25. Also, the narrow band gap of the mesoporous PtO−ZnO nanocomposites could create a wide effective visible region and thus build up their photocatalytic efficiency.[45] The second main reason is thought to be the mesostructure of the PtO−ZnO matrix with a high surface area. This is explained by the increase in TC adsorption, TC diffusion, and the number of active sites on the PtO−ZnO surface. It could be inferred that the PtO NPs incorporated on the ZnO surface acted as an effective cocatalyst and better electron sink, which could facilitate the separation of the photoinduced carrier. The ZnO and PtO NPs preserved the particles sizes of around 5−10 and 3 nm, respectively. The ZnO Fermi level was lower than that of PtO; the electric field was generated from the potential interaction barriers of the PtO−ZnO. These potential barriers support the transformation of photoelectrons from the conduction band of ZnO to PtO, inhibiting the recombination of carriers. PtO NPs (3 nm) can not only decrease the consumption of Pt but also help in effective electron trapping, thus enhancing the charge carrier separation. Besides, the strong interaction between PtO and ZnO could also have contributed to the charge separation through TC degradation.[46]

The influence of the loading amount of mesoporous 0.6% PtO−ZnO nanocomposite (0.6−3 g L^{-1}) was determined

https://dx.doi.org/10.1021/acsomega.1c00135
ACS Omega 2021, 6, 6438−6447

from the TC photodegradation efficiency (Figure 7a). The results revealed a linear improvement of TC degradation by

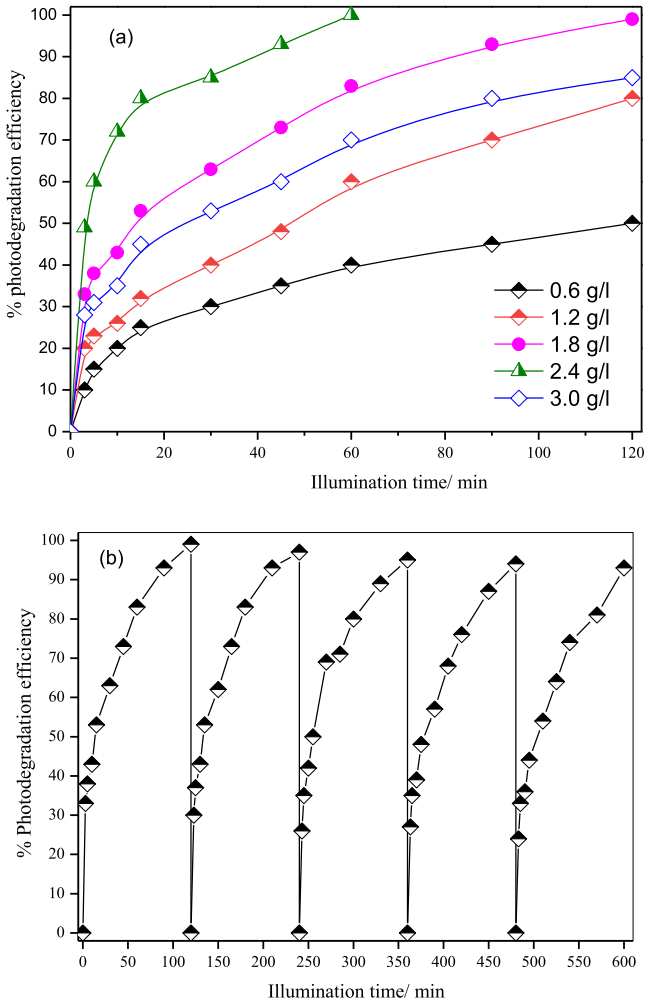

Figure 7. (a) Effect of the loading amount of 0.6 wt % PtO−ZnO nanocomposite on the photodegradation of tetracycline. (b) Time courses for recyclability of the photodegradation of tetracycline for 5 times over the mesoporous 0.6 wt % PtO−ZnO nanocomposite.

increasing the loading amount of PtO−ZnO nanocomposite from 0.6 to 1.8 g L^{-1}. The increase of TC degradation efficiency is associated with the comparable widening of accessible active sites for the reactant and light adsorption. By increasing the loading amount of PtO−ZnO from 0.6 to 1.8 g L^{-1}, the TC degradation efficiency enhanced significantly from 50 to 99%, respectively. However, at a high loading amount of the photocatalyst, the TC degradation efficiency was minimized to 85% at 3 g L^{-1} due to the increment turbidity of the solution, which is considered as one of the foremost reasons for reduction of the TC degradation efficiency. Besides, the increment turbidity of the solution led to the light scattering and hence the loss of light energy. In general, the light scattering resulting from the suspended photocatalyst reduces the light transmission, resulting in an inadequate TC degradation. Besides photocatalytic performance, stability and reusability are indispensable for photocatalyst applications. As depicted in Figure 7b, repeated TC degradation over five cycles demonstrated that the 0.6% PtO−ZnO nanocomposite exhibited good stability for the TC degradation under similar conditions. A much higher (95%) TC degradation efficiency could be achieved after recycling for five times. It is revealed that the PtO−ZnO nanocomposite is preserved through five-times-recycled photodegradation of TC. According to our current research, the mesoporous PtO−ZnO nanocomposite with structural stability and high photocatalytic performance could be anticipated as an excellent promising photocatalyst for practical applications.

To further prove the effective separation and migration of photo-created carriers on mesoporous PtO−ZnO photocatalysts, photoluminescence spectra and transient photocurrent measurements were taken as shown in Figure 8. As

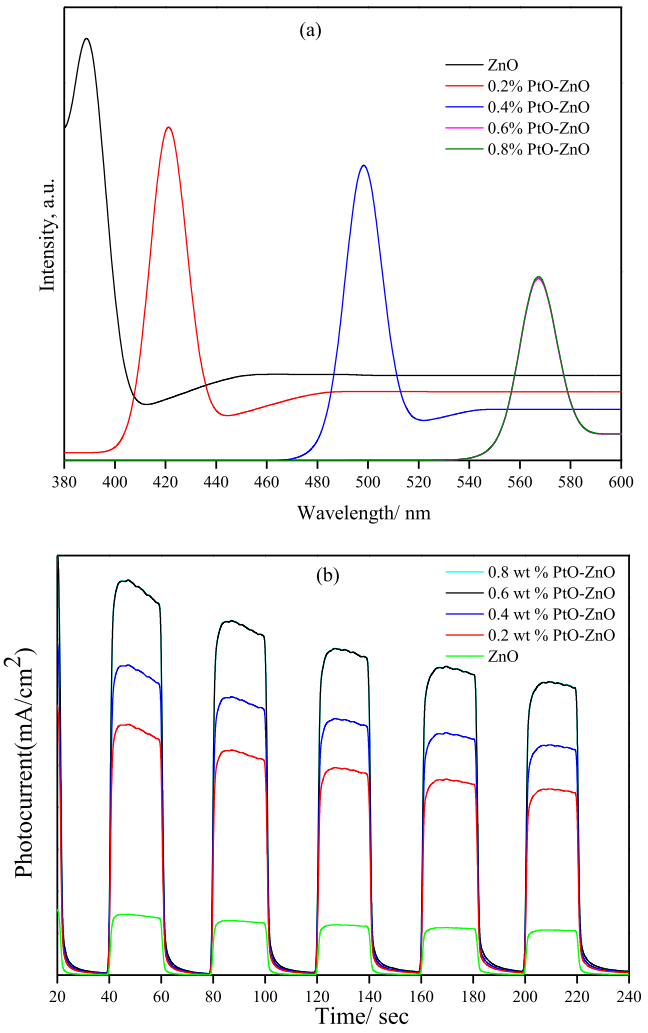

Figure 8. (a) PL spectra of mesoporous ZnO NPs and mesoporous PtO−ZnO nanocomposites at varying PtO contents (0.2−0.8 wt %). (b) Transmission efficiency of the photoexcited electrons in mesoporous ZnO NPs and mesoporous PtO−ZnO nanocomposites at varying PtO contents (0.2−0.8 wt %).

depicted in Figure 8a, the mesoporous PtO−ZnO nanocomposite at diverse PtO percentages revealed a highly reduced-intensity PL compared to pristine ZnO NPs, indicating the efficacious prohibition of the recombination of photoinduced electrons and holes in these nanocomposites. Note that the PL of pristine ZnO NPs appeared at $\lambda \sim 388$ nm; however, the PL intensity of the PtO−ZnO nanocomposite at diverse PtO percentages still obviously decreased and red-shifted to 421, 497, 567, and 567 nm for mesoporous

https://dx.doi.org/10.1021/acsomega.1c00135
ACS Omega 2021, 6, 6438−6447

0.2, 0.4, 0.6, and 0.8% PtO−ZnO nanocomposites, indicating that the much higher photocatalytic performance of the 0.6 and 0.8% PtO−ZnO nanocomposites is explained by the restraining of the electron and hole recombination. Also, the transient photocurrent response shown in Figure 8b indicates that the PtO−ZnO nanocomposites produced a constant transient photocurrent through five discontinuous illumination cycles. All PtO−ZnO nanocomposites and pristine ZnO NPs displayed instantaneous responses to light. The results indicated that the photocurrent responses of the 0.6 and 0.8% PtO−ZnO nanocomposites are the highest, suggesting that the recombination rate of the carriers is low. The photocurrent intensity followed the sequence 0.8% PtO−ZnO = 0.6% PtO−ZnO > 0.4% PtO−ZnO > 0.2% PtO−ZnO > ZnO. Particularly, the findings of photocurrent response and PL measurements are consistent with the photocatalytic performances; PtO−ZnO heterojunctions could thus enhance the effective transfer and separation of photoinduced electrons and holes and exhibited an outstanding photocatalytic effect. These phenomena show that the recombination rate of carriers could be prohibited by incorporation of PtO NPs on the ZnO matrix.

A photocatalytic mechanism of the mesoporous PtO−ZnO photocatalyst was suggested according to the above results for TC degradation (Scheme 1). The mesoporous PtO−ZnO network facilitates the mass transfer of TC molecules. The incorporation of PtO NPs on the mesoporous ZnO matrix could improve its photocatalytic efficiency, as shown by the obvious construction of close contacts between the PtO and ZnO NPs in the TEM images (Figure 4d) that facilitates the immigration of charge carriers. Upon illumination, ZnO can be photo-excited to create the electrons and holes on the PtO−ZnO surface. The photoinduced electrons are transferred to PtO to form a superoxide radical; Pt^{2+} doping reduces the band gap of ZnO to enhance light absorption.[46] The photoinduced electrons might reduce O_2 to yield $^{\bullet}O_2^-$ in the reaction solution and subsequently the protonation of $^{\bullet}O_2^-$ might produce $HO_2^{\bullet}$ radicals, leading to the H_2O_2 formation. The formed H_2O_2 molecules could react with the excess electrons to produce the highly oxidizing $^{\bullet}OH$ radicals. On the other side, the photoinduced holes are easily trapped by the adsorbed H_2O/OH^- to yield $^{\bullet}OH$; then the TCs are degraded to the environment-friendly CO_2 and H_2O by the $^{\bullet}OH$, $^{\bullet}O_2^-$ radical, and holes. Obviously, the reactive species generated through the photocatalysis reaction are concomitantly excited, including the $^{\bullet}O_2^-$, h^+, and $^{\bullet}OH$ in the reaction solution.

Scheme 1. Schematic Elucidation of the Photocatalytic Reaction Mechanism for TC Degradation over Mesoporous PtO−ZnO Nanocomposites

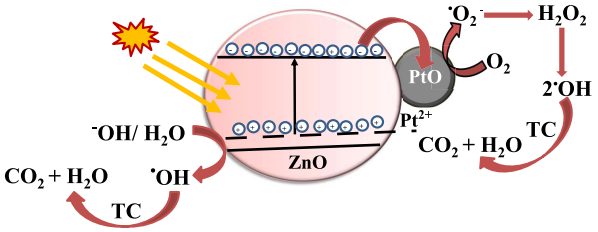

4. CONCLUSIONS

In summary, we report a simple method of incorporation of PtO NPs onto a highly crystalline and mesoporous ZnO matrix by the wet-impregnation approach for degradation of tetracycline (TC) upon visible light exposure. The uniform crystal structure of the mesoporous ZnO matrix with high crystallinity contributes to the construction of PtO NPs on the ZnO matrix with high dispersity and small size. The resultant mesoporous PtO−ZnO nanocomposites exhibit a significant enhancement of photocatalytic efficiency for TC degradation compared with commercial P-25 and pristine ZnO NPs. The optimized 0.6% PtO−ZnO photocatalyst exhibits an excellent degradation efficiency of TC, reaching ∼99%. The photocatalytic efficiency is observed to follow the trend 0.8% PtO−ZnO ≥ 0.6% PtO−ZnO > 0.4% PtO−ZnO > 0.2% PtO−ZnO > TiO_2-P25 > ZnO NPs. The rate constant value of the 0.6% PtO−ZnO nanocomposite was 48 and 18 times higher than that for pristine ZnO NPs and commercial P-25, respectively. These mesoporous PtO−ZnO nanocomposites showed excellent photocatalytic performance due to their more effective separation of photoinduced electrons and holes, small particle sizes, and larger surface area. Accordingly, mesoporous PtO−ZnO nanocomposites with structural stability and high photocatalytic performance could be anticipated as excellent promising photocatalysts for practical application.

AUTHOR INFORMATION

Corresponding Authors

Reda M. Mohamed − *Department of Chemistry, Faculty of Science, King Abdulaziz University, Jeddah 21589, Kingdom of Saudi Arabia; Advanced Materials Department, Central Metallurgical R&D Institute, CMRDI, Helwan, Cairo 11421, Egypt;* orcid.org/0000-0002-6182-6880; Email: redama123@yahoo.com

Adel A. Ismail − *Advanced Materials Department, Central Metallurgical R&D Institute, CMRDI, Helwan, Cairo 11421, Egypt; Nanotechnology and Advanced Materials Program, Energy & Building Research Center, Kuwait Institute for Scientific Research (KISR), Safat 13109, Kuwait;* orcid.org/0000-0002-5227-2644; Email: adelali141@yahoo.com

Authors

Mohammad W. Kadi − *Department of Chemistry, Faculty of Science, King Abdulaziz University, Jeddah 21589, Kingdom of Saudi Arabia*

Ajayb S. Alresheedi − *Department of Chemistry, Faculty of Science, King Abdulaziz University, Jeddah 21589, Kingdom of Saudi Arabia*

Ibraheem A. Mkhalid − *Department of Chemistry, Faculty of Science, King Abdulaziz University, Jeddah 21589, Kingdom of Saudi Arabia*

Complete contact information is available at: https://pubs.acs.org/10.1021/acsomega.1c00135

Notes

The authors declare no competing financial interest.

ACKNOWLEDGMENTS

This project was funded by the Deanship of Scientific Research (DSR) at King Abdulaziz University, Jeddah, Saudi Arabia

https://dx.doi.org/10.1021/acsomega.1c00135
ACS Omega 2021, 6, 6438−6447

under grant no. KEP-PhD-7-130-41. The authors, therefore, thank the DSR for technical and financial support.

REFERENCES

(1) Popugaeva, D.; Tian, T.; Ray, A. K. Hydrogen production from aqueous triethanolamine solution using Eosin Y-sensitized ZnO photocatalyst doped with platinum. *Int. J. Hydrogen Energy* **2020**, *45*, 11097−11107.
(2) Faisal, M.; Khan, S. B.; Rahman, M. M.; Ismail, A. A.; Asiri, A. M.; Al-Sayari, S. A. Development of efficient chemi-sensor and photocatalyst based on wet-chemically prepared ZnO nanorods for environmental remediation. *J. Taiwan Inst. Chem. Eng.* **2014**, *45*, 2733−2741.
(3) Desai, M. A.; Vyas, A. N.; Saratale, G. D.; Sartale, S. D. Zinc oxide superstructures: recent synthesis approaches and application for hydrogen production via photoelectrochemical water splitting. *Int. J. Hydrogen Energy* **2019**, *44*, 2091−2127.
(4) Faisal, M.; Ibrahim, A. A.; Harraz, F. A.; Bouzid, H.; Al-Assiri, M. S.; Ismail, A. A. SnO_2 doped ZnO nanostructures for highly efficient photocatalyst. *J. Mol. Catal. A: Chem.* **2015**, *397*, 19−25.
(5) Kostedt, W. L.; Ismail, A. A.; Mazyck, D. W. Impact of heat treatment and composition of ZnO-TiO_2 nanoparticles for photocatalytic oxidation of an Azo dye. *Ind. Eng. Chem. Res.* **2008**, *47*, 1483−1487.
(6) Fouad, O. A.; Ismail, A. A.; Zaki, Z. I.; Mohamed, R. M. Zinc oxide thin films prepared by thermal evaporation deposition and its photocatalytic activity. *Appl. Catal., B* **2006**, *62*, 144−149.
(7) Kegel, J.; Povey, I. M.; Pemble, M. E. Zinc oxide for solar water splitting: a brief review of the material's challenges and associated opportunities. *Nano Energy* **2018**, *54*, 409−428.
(8) George, L.; Sappati, S.; Ghosh, P.; Devi, R. N. Surface site modulations by conjugated organic molecules to enhance visible light activity of ZnO nanostructures in photocatalytic water splitting. *J. Phys. Chem. C* **2015**, *119*, 3060−3067.
(9) He, L.; Dou, X.; Li, X.; Qin, L.; Kang, S. Z. Remarkable enhancement of the photocatalytic activity of ZnO nanorod array byutilizing energy transfer between Eosin Y and Rose Bengal for visible light-driven hydrogen evolution. *Int. J. Hydrogen Energy* **2018**, *43*, 15255−15261.
(10) Ali, A. M.; Ismail, A. A.; Najmy, R.; Al-Hajry, A. Preparation and characterization of ZnO/SiO_2 films as highly efficient photocatalyst. *J. Photochem. Photobiol., A* **2014**, *275*, 37−46.
(11) Chowdhury, P.; Gomaa, H.; Ray, A. K. Sacrificial hydrogen generation from aqueous triethanolamine with Eosin Y sensitized Pt/TiO_2 photocatalyst in UV, visible and solar light irradiation. *Chemosphere* **2015**, *121*, 54−61.
(12) Saraswat, S. K.; Rodene, D. D.; Gupta, R. B. Recent advancements in semiconductor materials for photoelectrochemical water splitting for hydrogen production using visible light. *Renewable Sustainable Energy Rev.* **2018**, *89*, 228−248.
(13) Li, J.; Fan, H.; Jia, X. Multilayered ZnO nanosheets with 3D porous architectures: Synthesis and gas sensing application. *J. Phys. Chem. C* **2010**, *114*, 14684−14691.
(14) Ma, L.; Fan, H.; Tian, H.; Fang, J.; Qian, X. The n-ZnO/n-In_2O_3 heterojunction formed by a surface-modification and their potential barrier-control in methanal gas sensing. *Sens. Actuators, B* **2016**, *222*, 508−516.
(15) Wang, C.; Fan, H.; Ren, X.; Wen, Y.; Wang, W. Highly dispersed PtO nanodots as efficient co-catalyst for photocatalytic hydrogen evolution. *Appl. Surf. Sci.* **2018**, *462*, 423−431.
(16) Wang, H.; Li, Q.; Zheng, X.; Wang, C.; Ma, J.; Yan, B.; Du, Z.; Li, M.; Wang, W.; Fan, H. 3D porous flower-like ZnO microstructures loaded by large-size Ag and their ultrahigh sensitivity to ethanol. *J. Alloys Compd.* **2020**, *829*, No. 154453.
(17) Campelo, J. M.; Luna, D.; Luque, R.; Marinas, J. M.; Romero, A. A. Sustainable preparation of supported metal nanoparticles and their applications in catalysis. *ChemSusChem* **2009**, *2*, 18−45.
(18) Fan, Z.; Zhang, H. Template Synthesis of noble metal nanocrystals with unusual crystal structures and their catalytic applications. *Acc. Chem. Res.* **2016**, *49*, 2841−2850.
(19) Huang, J.; Zhu, Y.; Lin, M.; Wang, Q.; Zhao, L.; Yang, Y.; Yao, K. X.; Han, Y. Site-specific growth of Au-Pd alloy horns on Aunanorods: a platform for highly sensitive monitoring of catalytic reactions by surface enhancement Raman spectroscopy. *J. Am. Chem. Soc.* **2013**, *135*, 8552−8561.
(20) Manwar, N. R.; Chilkalwar, A. A.; Nanda, K. K.; Chaudhary, Y. S.; Subrt, J.; Rayalu, S. S.; Labhsetwar, N. K. Ceria Supported Pt/PtO-Nanostructures: Efficient Photocatalyst for Sacrificial Donor Assisted Hydrogen Generation under Visible-NIR Light Irradiation. *ACS Sustainable Chem. Eng.* **2016**, *4*, 2323−2332.
(21) Huang, D. B.; Yuan, Q.; He, P. L.; Wang, K.; Wang, X. A facile and general strategy for the synthesis of porous flowerlike Pt-based nanocrystals as effective electrocatalysts for alcohol oxidation. *Nanoscale* **2016**, *8*, 14705−14710.
(22) Zeng, H.; Liu, P.; Cai, W.; Yang, S.; Xu, X. Controllable Pt/ZnO Porous Nanocages with Improved Photocatalytic Activity. *J. Phys. Chem. C* **2008**, *112*, 19620−19624.
(23) Yang, X.; Li, Y.; Zhang, P.; Zhou, R.; Peng, H.; Liu, D.; Gui, J. Photoinduced in situ deposition of uniform and well-dispersed PtO_2 nanoparticles on ZnO Nanorods for efficient catalytic reduction of 4-nitrophenol. *ACS Appl. Mater. Interfaces* **2018**, *10*, 23154−23162.
(24) Mohamed, R. M.; Ismail, A. A.; Kadi, M. W.; Alresheedi, A. S.; Mkhalid, I. A. Facile Synthesis of mesoporous Ag_2O-ZnO nanocomposites for enhancement of visible light photocatalytic efficiency. *ACS Omega* **2020**, *5*, 33269−33279.
(25) Bouzid, H.; Faisal, M.; Harraz, F. A.; Al-Sayari, S. A.; Ismail, A. A. Synthesis of mesoporous Ag/ZnO nanocrystals with enhanced photocatalytic activity. *Catal. Today* **2015**, *252*, 20−26.
(26) Faisal, M.; Bouzid, H.; Harraz, F. A.; Al-Sayari, S. A.; Al-Assiri, M. S.; Ismail, A. A. Mesoporous Ag/ZnO multilayer films prepared by repeated spin-coating for enhancing its photonic efficiencies. *Surf. Coat. Technol.* **2015**, *263*, 44−53.
(27) Yu, H.; Shi, R.; Zhao, Y.; Waterhouse, G. I.; Wu, L. Z.; Tung, C. H.; Zhang, T. Smart Utilization of Carbon Dots in Semiconductor Photocatalysis. *Adv. Mater.* **2016**, *28*, 9454−9477.
(28) Chen, X.; Shen, S.; Guo, L.; Mao, S. S. Semiconductor-Based Photocatalytic Hydrogen Generation. *Chem. Rev.* **2010**, *110*, 6503−6570.
(29) Jiang, W.; Liu, Y.; Zong, R.; Li, Z.; Yao, W.; Zhu, Y. Photocatalytic hydrogen generation on bifunctional ternary heterostructured In_2S_3/MoS_2/CdS composites with high activity and stability under visible light irradiation. *J. Mater. Chem. A* **2015**, *3*, 18406−18412.
(30) Cao, B.; Li, G.; Li, H. Hollow spherical RuO_2@TiO_2@Pt bifunctional photocatalyst for coupled H_2 production and pollutant degradation. *Appl. Catal., B* **2016**, *194*, 42−49.
(31) Xiang, Q.; Yu, J.; Jaroniec, M. Synergetic effect of MoS_2 and graphene as cocatalysts for enhanced photocatalytic H_2 production activity of TiO_2 nanoparticles. *J. Am. Chem. Soc.* **2012**, *134*, 6575−6578.
(32) Zhang, P.; Yang, X.; Zhao, Z.; Li, B.; Gui, J.; Liu, D.; Qiu, J. One-step synthesis of flowerlike C/Fe_2O_3 nanosheet assembly with superior adsorption capacity and visible light photocatalytic performance for dye removal. *Carbon* **2017**, *116*, 59−67.
(33) Zhang, P.; Chen, Y.; Yang, X.; Gui, J.; Li, Y.; Peng, H.; Liu, D.; Qiu, J. Pt/ZnO@C Nanocable with Dual-Enhanced Photocatalytic Performance and Superior Photostability. *Langmuir* **2017**, *33*, 4452−4460.
(34) Zhang, P.; Li, B.; Zhao, Z.; Yu, C.; Hu, C.; Wu, S.; Qiu, J. Furfural-induced hydrothermal synthesis of ZnO@C gemel hexagonalmicrorods with enhanced photocatalytic activity and stability. *ACS Appl. Mater. Interfaces* **2014**, *6*, 8560−8566.
(35) Wang, H.; Zhang, L.; Chen, Z.; Hu, J.; Li, S.; Wang, Z.; Liu, J.; Wang, X. Semiconductor heterojunction photocatalysts: design, construction, and photocatalytic performances. *Chem. Soc. Rev.* **2014**, *43*, 5234−8244.

https://dx.doi.org/10.1021/acsomega.1c00135
ACS Omega 2021, 6, 6438−6447

(36) Philip, J. M.; Aravind, U. K.; Aravindakumar, C. T. Emerging contaminants in Indian environmental matrices – A review. *Chemosphere* **2018**, *190*, 307–326.
(37) Ji, L.; Chen, W.; Duan, L.; Zhu, D. Mechanisms for strong adsorption of tetracycline to carbon nanotubes: a comparative study using activated carbon and graphite as adsorbents. *Environ. Sci. Technol.* **2009**, *43*, 2322–2327.
(38) Jin, C.; Li, W.; Chen, Y.; Li, R.; Huo, J.; He, Q.; Wang, Y. Efficient Photocatalytic Degradation and adsorption of tetracycline over type-II heterojunctions consisting of ZnO nanorods and K-doped exfoliated g-C_3N_4 nanosheets. *Ind. Eng. Chem. Res.* **2020**, *59*, 2860–2873.
(39) Yan, X.; Yuan, K.; Lu, N.; Xu, H.; Zhang, S.; Takeuchi, N.; Kobayashi, H.; Li, R. The interplay of sulfur doping and surface hydroxyl in band gap engineering: Mesoporous sulfur-doped TiO_2 coupled with magnetite as a recyclable, efficient, visible light active photocatalyst for water purification. *Appl. Catal., B* **2017**, *218*, 20–31.
(40) Weng, B.; Yang, M. Q.; Zhang, N.; Xu, Y. J. Toward the enhanced photoactivity and photostability of ZnO nanospheres via intimate surface coating with reduced graphene oxide. *J. Mater. Chem. A* **2014**, *2*, 9380–9389.
(41) Gregg, S. J.; Sing, K. S. W. *Adsorption, Surface Area and Porosity*; Academic Press: London, 1982.
(42) Chen, L. F.; Zhou, X. L.; Norena, L. E.; Wang, J. A.; Navarrete, J.; Salas, P.; Montoya, A.; Angel, P. D.; Llanos, M. E. Comparative studies of Zr-based MCM-41 and MCM-48 mesoporous molecular sieves: Synthesis and physicochemical properties. *Appl. Surf. Sci.* **2006**, *253*, 2443–2451.
(43) Zhu, W.; Zhang, X.; Wang, X.; Zhang, H.; Zhang, Q.; Xiang, L. Short belt-like $Ca_2B_2O_5{\cdot}H_2O$ nanostructures: Hydrothermal formation, FT-IR, thermal decomposition, and optical properties. *J. Cryst. Growth* **2011**, *332*, 81–86.
(44) Khataee, A.; Darvishi Cheshmeh Soltani, R.; Hanifehpour, Y.; Safarpour, M.; Gholipour, R. H.; Joo, S. W. Synthesis and characterization of dysprosium-doped ZnO nanoparticles for photocatalysis of a textile dye under visible light irradiation. *Ind. Eng. Chem. Res.* **2014**, *53*, 1924–1932.
(45) Jiang, J.; Yu, J.; Cao, S. Au/PtO nanoparticle-modified g-C_3N_4 for plasmon-enhanced photocatalytic hydrogen evolution under visible light. *J. Colloid Interface Sci.* **2016**, *461*, 56–63.
(46) Wang, C.; Fan, H.; Ren, X.; Wen, Y.; Wang, W. Highly dispersed PtO nanodots as efficient co-catalyst for photocatalytic hydrogen evolution. *Appl. Surf. Sci.* **2018**, *462*, 423–431.
(47) Li, N.; Tian, Y.; Zhao, J.; Zhan, W.; Du, J.; Kong, L.; Zhang, J.; Zuo, W. Ultrafast selective capture of phosphorus from sewage by 3D Fe_3O_4@ZnO via weak magnetic field enhanced adsorption. *Chem. Eng. J.* **2018**, *341*, 289–297.
(48) Ismail, A. A.; Harraz, F. A.; Faisal, M.; El-Toni, A. M.; Al-Hajry, A.; Al-Assiri, M. S. A sensitive and selective amperometric hydrazine sensor based on mesoporous Au/ZnO nanocomposites. *Mater. Des.* **2016**, *109*, 530–538.
(49) Ismail, A. A.; Bahnemann, D. W.; Robben, L.; Yarovyi, V.; Wark, M. Palladium doped porous titania photocatalysts: Impact of mesoporous order and crystallinity. *Chem. Mater.* **2010**, *22*, 108–116.

https://dx.doi.org/10.1021/acsomega.1c00135
ACS Omega 2021, 6, 6438–6447